A magnetic cloud prediction model for forecasting space weather relevant properties of Earth-directed coronal mass ejections

Sanchita Pal[1,2], Dibyendu Nandy[1,3], and Emilia K. J. Kilpua[2]

[1] Center of Excellence in Space Sciences India, Indian Institute of Science Education and Research Kolkata, Mohanpur 741246, West Bengal, India
[2] Department of Physics, University of Helsinki, P.O. Box 64, FI-00014 Helsinki, Finland
[3] Department of Physical Sciences, Indian Institute of Science Education and Research Kolkata, Mohanpur 741246, West Bengal, India
e-mail: sanchita.pal@helsinki.fi

March 11, 2022

ABSTRACT

Context. Coronal Mass Ejections (CMEs) are energetic storms in the Sun that result in the ejection of large-scale magnetic clouds (MCs) in interplanetary space that contain enhanced magnetic fields with coherently changing field direction. The severity of CME induced geomagnetic perturbations depends on the direction and strength of the interplanetary magnetic field (IMF), as well as the speed and duration of passage of the magnetic cloud associated with the storm. The coupling between the heliospheric environment and Earth's magnetosphere is the strongest when the IMF direction is persistently southward for a prolonged period. Predicting the magnetic profile of such Earth-directed CMEs is crucial for estimating their geomagnetic impact; this remains an outstanding challenge.
Aims. Our aim is to build upon and integrate diverse techniques towards development of a comprehensive magnetic cloud prediction (MCP) model that can forecast the magnetic field vectors, Earth-impact time, speed and duration of passage of solar storms.
Methods. The configuration of a CME is approximated as a radially expanding force-free cylindrical structure. Combining near-Sun geometrical, magnetic and kinematic properties of CMEs with the probabilistic drag based model and cylindrical force-free model we propose a methodology for predicting the Earth-arrival time, propagation speed, and magnetic vectors of MCs during their passage through 1 AU. A novelty of our scheme is the ability to predict the passage duration of the storm without recourse to computationally intensive, time-dependent dynamical equations.
Results. Our methodology is validated by comparing the MCP model output with observations of ten MCs at 1 AU. In our sample, we find that eight MCs show a root mean square (rms) deviation of less than 0.1 between predicted and observed magnetic profiles and the passage duration of seven MCs fall within the predicted range.
Conclusions. Based on the success of this approach, we conclude that predicting the near-Earth properties of MCs based on analysis and modelling of near-Sun CME observations is a viable endeavor with potential benefits for space weather assessment.

Use \titlerunning to supply a shorter title and/or \authorrunning to supply a shorter list of authors.

1. Introduction

Understanding space weather and its variability has become increasingly important as we rely more and more on the space-borne technology and interconnected power-grids which are sensitive to disturbance from the Sun (e.g., Schrijver et al. 2015). Coronal mass ejections (CMEs; Webb & Howard 2012) are one of the most important drivers of severe space weather events. Their flux rope (FR) structures can be observed in white-light coronagraphs near-Sun (e.g., Vourlidas et al. 2017), and in situ observation in interplanetary space (e.g., Kilpua et al. 2017). When the twisted magnetic FR of a CME contains southward magnetic field components, magnetic reconnection with the Earth's magnetosphere ensues and leads to effective solar wind mass, momentum, and energy transfer to the Earth's magnetosphere. This generates significant ring current enhancement and results in a geomagnetic storm (Tsurutani et al. 1988; Gonzalez et al. 1999). Therefore, prior knowledge of the magnetic properties of Earth-directed CMEs is crucial for reliably predicting their geoeffectiveness and space weather impacts.

The first step in estimating the geomagnetic response for a given CME is to estimate its initial parameters including their structure, propagation direction, kinematics and magnetic properties, soon after their origin at the Sun. Depending on the location of the CME source, CME properties are subject to projection effect (Burkepile et al. 2004; Howard et al. 2008). Applying forward modelling technique (Thernisien et al. 2006) to white-light CMEs observed simultaneously from different vantage points in space, one can reproduce CME's 3D morphology and estimate deprojected geometrical parameters and kinematics (Bosman et al. 2012; Shen et al. 2013). The next step is to evaluate how the initial parameters evolve after the CME is launched from the Sun. CMEs can experience changes in their space weather relevant properties and propagation direction (e.g., Manchester et al. 2017; Kilpua et al. 2019). Firstly, CMEs expand during their interplanetary propagation (Burlaga et al. 1981; Burlaga 1991). A study by Démoulin & Dasso (2009) demonstrates that the rapid decrease of solar wind pressure with increasing distance from the Sun is the main driver of the radial expansion of CMEs. The deflection of a CME can change significantly the latitude and longitude of its propagation

direction (Isavnin et al. 2014; Kay & Opher 2015). In addition, CMEs can experience fast and large rotation (e.g., Vourlidas et al. 2011; Isavnin et al. 2014). These are common phenomena in the solar corona due to the presence of strong magnetic forces (Isavnin et al. 2014; Kay et al. 2015). Deflections and rotations occur also further out in interplanetary space due to the interaction of a CME with the background solar wind magnetic fields (Wang et al. 2004) and preceding or following CMEs (Wang et al. 2004, 2014). Deflections can cause CMEs that were initially not heading towards the Earth to impact us or re-route Earth-directed CMEs away from our planet (e.g., Möstl et al. 2015). The rotation in turn changes the magnetic field profile finally impacting the Earth, and thus influences the geoeffectivity (Palmerio et al. 2018). Interaction of a CME FR with the ambient open flux may also result in flux erosion impacting geoeffectiveness (Pal et al. 2020). All of these phenomena is a challenge for the prediction of near-Earth CME properties, which nonetheless, is highly desirable.

The distortion of CME's geometrical structure can be observed in coronagraphs. However, the influence of distortion on CME's magnetic structure is hard to estimate because the magnetic field cannot yet be reliably measured in the hot and tenuous corona. To estimate CME's magnetic vectors few studies use solar observations as input to three-dimensional magnetohydrodynamic (MHD) models of CME evolution (Manchester et al. 2004; Shen et al. 2014). Although data driven physical MHD models for CME flux rope strucure prediction are desirable from the intellectual perspective, such models are computationally expensive (Manchester et al. 2014) and does not have enough observations in the inner heliosphere to constrain their evolution.

Various alternative semi-empirical modelling approaches have been proposed for prediction of the magnetic structure of CMEs. Using analytical and semi-analytical models which approximate CMEs as force-free cylindrical flux-ropes, several studies have performed predictions of the magnetic structure of CME flux ropes as they arrive near the Earth's orbit (Savani et al. 2015; Kay & Gopalswamy 2017; Möstl et al. 2018; Sarkar et al. 2020). One key aspect of these models is to constrain the magnetic properties of the CME flux rope as it leaves the Sun. Most models use as default the "Bothmer-Schwenn" scheme (Bothmer & Schwenn 1998). This scheme relies on hemispheric helicity rule (Pevtsov & Balasubramaniam 2003), which states that the northern (southern) hemisphere is dominated by magnetic structures with negative (positive) helicity sign and assumes that the orientation of the flux rope's axial field follows the polarity of the leading and trailing flux systems in active regions. The hemispheric rule applies only in a statistical sense and intrinsic AR magnetic properties such as tilt orientation and twist themselves have a large scatter (Nandy 2006). Models of coronal field evolution and CME genesis based on active regions properties often miss out a large proportion of events (Yeates et al. 2010) implying a gap in our understanding. A study by Liu et al. (2014) showed that in only 60% of the case the hemispheric helicity rule is followed in predicting the CME's flux rope chirality. In addition, rising CME flux ropes interact with overlying coronal fields and this interaction is cycle phase dependent (Cook et al. 2009). This may alter the amount of magnetic flux and helicity as they reconnect with the overlying coronal arcades during the CME lift-off. These further compound the problem of predictions.

Some approaches have been proposed recently to make headway in the face of these challenges. The Interplanetary Flux ROpe Simulator (INFROS) developed by Sarkar et al. (2020) determines the axial field direction, intensity and helicity sign using extreme ultraviolet (EUV), H-alpha and magnetogram observations of their sources. This approach allows constraining the flux rope parameters in a more realistic manner for event to event basis (see also Palmerio et al. 2017; Kilpua et al. 2019; Pal 2021). Most models mentioned above also take into account the expanding nature of the CME's flux rope as it crosses the observing spacecraft in interplanetary space. These models however utilize observed in situ values (speed, expansion speed) to estimate the expansion, and consequently the flux rope duration and thus the time window for predictions is very short.

In this paper we present a comprehensive empirical modelling framework that builds upon our knowledge to predict various space weather relevant characteristics of a CME magnetic cloud near Earth. The model, which we name the CESSI-MCP model has some unique characteristics, a particular novelty being that we utilize the CME's arrival time and speed along with considerations of self-similar expansion to predict the passage duration of the MC. In Section 2 we describe the model and outline procedures for estimating the model inputs. In Section 3 we validate our model using in situ observed MC events. The results are critically assessed in Section 4 and we conclude with a summary discussion in Section 5.

2. Methodology: Modeling MCs

2.1. MCP model description

To examine the configuration of MCs we assume them to be force free (Goldstein 1983), i.e., $\mathbf{J} = \alpha\mathbf{B}$, where $\mathbf{J}$ and $\mathbf{B}$ represent the current density and magnetic field vector, respectively. Marubashi (1986) used first the model allowing α to vary with the distance from the MC centre to fit two MCs. Later, Burlaga (1988) showed that α can be considered as constant to describe a magnetic cloud in the first order. For constant α the solutions of the force-free model in cylindrical co-ordinates are obtained by Lundquist (1951), where the axial (B_{ax}), azimuthal (B_{az}), and radial (B_{rad}) magnetic field components are given by,

$$B_{ax} = B_0 J_0(\alpha\rho), \tag{1}$$

$$B_{az} = H B_0 J_1(\alpha\rho), \tag{2}$$

and

$$B_\rho = 0, \tag{3}$$

respectively. In Equation 2 H represents the chirality of cylindrical FRs. The right and left-handed chirality of FRs are indicated by $H = 1$ and $H = -1$, respectively. The axial magnetic field intensity of FRs is represented by B_0. The zeroth and first order Bessel

functions of first kind are shown by J_0 and J_1, respectively. The parameter ρ is the radial distance from MC axis, and α is related to FR size. The value of α is chosen so that $\alpha R_{MC} = 2.41$, where 2.41 is the first zero of J_0 and R_{MC} is the radius of MC.

The field configuration described in Equation 1 and 2 is static. Burlaga et al. (1981); Burlaga (1991) indicated the expanding nature of MCs causing smooth decrease in solar wind speed and low solar wind proton temperature during their intervals. Démoulin et al. (2008); Démoulin & Dasso (2009) performed theoretical studies on the expansion of MCs. The studies concluded that MCs expand self-similarly resulting in a linear radial velocity profile of MCs and the rate of MC expansion is proportional to the MC radius. The expansion of MC was first modeled by Osherovich et al. (1993) later followed by other studies, including, Marubashi (1997); Hidalgo (2003); Vandas et al. (2006), and Marubashi & Lepping (2007). These models are intended to fit the velocity magnitude profile of MCs. It is assumed that in an asymptotic limit, an FR expands radially with a speed

$$V_{exp} = \frac{\rho}{t + t_0}, \tag{4}$$

where the force free field configuration is maintained at any instant of time t (Shimazu & Vandas 2002; Vandas et al. 2006, 2015). In a self-similar expansion, the t_0 in Equation 4 represents the time by which the expansion of FR has proceeded before it comes into contact with the spacecraft. If a self-similarly expanding MC changes its radius from its initial value $R_{MC}(0)$ to $R_{MC}(t)$ by the time t, the $R_{MC}(t)$ can be represented as $R_{MC}(t) = R_{MC}(0)(1 + \frac{t}{t_0})$. Thus, for an expanding FR, α and B_0 become time-dependent and are expressed as $\alpha = \frac{\alpha_0}{(1 + \frac{t}{t_0})}$ and $B_0 = \frac{B_0'}{(1 + \frac{t}{t_0})^2}$, where $\alpha_0 = 2.41/R_{MC}(0)$ and B_0' is the axial magnetic field intensity when the MC first encounters with the spacecraft. Considering the expansion of the MC along radial and axial directions Equation 1 & 2 are modified as

$$B_{ax} = \frac{B_0' J_0(\frac{\alpha_0}{(1 + \frac{t}{t_0})}\rho)}{(1 + \frac{t}{t_0})^2}, \tag{5}$$

$$B_{az} = H \frac{B_0' J_1(\frac{\alpha_0}{(1 + \frac{t}{t_0})}\rho)}{(1 + \frac{t}{t_0})^2}, \tag{6}$$

where the force free condition is assumed to be preserved throughout the propagation of MCs.

Knowledge of the perpendicular distance (p) between an MC axis and the location of a spacecraft performing the in situ measurements of the MC is necessary to obtain ρ. Figure 2 shows a cylindrical MC and its expanding cross-section. The MC expands with a velocity V_{exp} and its axis propagates with a speed V_{pro}. In the FR frame of reference it is assumed that the spacecraft propagates with the speed V_{pro}. At the in-bound and out-bound regions of the MC the V_{exp} is added to and subtracted from the ambient solar wind speed, respectively, to obtain V_{pro} (Vandas et al. 2015). For $0 < p < R_{MC}$ the $\rho(t) = \sqrt{p^2 + (D^2(t) - V_{pro}(t) \times t)}$, where $D(t) = \sqrt{R_{MC}^2(t) - p^2}$. Thus at $t = 0$, when an MC first encounters the spacecraft, $\rho(0) = R_{MC}(0)$. Figure 2 is shown in the FR frame of reference where the spacecraft traverses through the MC with a speed V_{pro}. The schematic shown in Figure 2(a) represents the crossing of a spacecraft through an MC via a path 'AC' indicated by black dash line. The MC axis is shown by a blue dashed line and the circumference of the MC cross-section is indicated by a red dashed circle. The centre of the MC is pointed by 'O', and 'OB' represents the distance p. In Figure 2(b) the expanding MC cross-section is shown. At $t = 0$, the circle made of solid red line represents the MC cross-section circumference where the distance 'AB' is equivalent to $D(0)$. Once we obtain the value of V_{exp} at $t = 0$, we can estimate t_0 value from $t_0 = V_{exp}^{t=0}/R_{MC}(0)$.

Several studies have related radial speed (V_{rad}) and expansion speed (V_{exp}) of CME's FRs at the near-Sun region (Dal Lago et al. 2003; Schwenn et al. 2005; Gopalswamy et al. 2012). As mentioned in the Introduction, the reason of CME's expansion is mainly the decaying solar wind pressure surrounding the CME. The expansion is rapid within a distance ≈ 0.4 AU from the Sun and becomes moderate at large distance (Scolini et al. 2021). Lepping et al. (2008) formulated the 'scalar derivation' of expansion speed of FRs near the Earth that uses FR width, propagation speed, and duration of FR passage. As the formulation depends on the unknown free parameters like FR duration, we utilise the value of FR average expansion speed at 1 AU estimated by previous statistical studies. Lepping et al. (2008) analysed 53 MCs of standard profiles and obtained their expansion speed using two different methods namely the "scalar" method and "vector determination". They found the most probable values of expansion speed to be around 30 km/s. Nieves-Chinchilla et al. (2018) studied a large number (337) of ICMEs observed by Wind spacecraft during 1995 - 2015 and reported that MC expansion speed ranges from - 56 to 271 km/s with the mean value of 28 km/s. Therefore, we consider the value of $V_{exp}^{t=0}$ as 28 km/s in our study.

To obtain the model parameters specifically p, R_{MC0}, B_0' and H the near-Sun observations of the associated CME FRs are utilized. As discussed in the Introduction, the significant deflection and rotation of CMEs regularly occur near the Sun, within $10R_\odot$ (Kay & Opher 2015; Lynch et al. 2009). We assume here that the propagation direction, axis orientation, and chirality of CMEs obtained at a height $> 10R_\odot$ remain unchanged throughout their Sun-Earth propagation. The radius and magnetic field intensity of CMEs are in turn assumed to evolve from their values approximated at $\sim 10R_\odot$ due to self-similar expansion (Subramanian et al. 2014; Vršnak et al. 2019) in the course of interplanetary propagation. In the following sections we discuss the procedures used in determination of model parameters.

2.2. Estimates of the geometrical properties of FRs

We estimate CME's three-dimensional morphology and propagation direction in the outer corona $\sim 10 - -25R_\odot$ by fitting the geometrical structure of CMEs using graduated cylindrical shell (GCS) model (Thernisien 2011). The CMEs are observed in C2 & C3 coronagraphs of Large Angle and Spectrometric Coronagraph (LASCO) telescope on board the Solar and Heliospheric Observatory (SOHO) and COR2 A & B of Sun Earth Connection Coronal and Heliospheric Investigation (SECCHI) on board the Solar Terrestrial Relations Observatory (STEREO). By fitting the CMEs with GCS model, we obtain the latitude (θ_{HG}) and longitude (ϕ_{HG}) of the apex of CMEs in Stonyhurst heliographic coordinates, the tilt η ($-90° < \eta < 90°$) of the axis of FR CMEs, aspect ratio (κ), height (h_l) of the CME leading edges and the angle (AW) formed between the two legs of CME FRs. The FR axis tilt η is measured as counterclockwise positive from the solar West direction. The uncertainty in determining η using GCS is $\pm10°$ (Thernisien et al. 2009). Sarkar et al. (2020) considered uncertainties of $\pm10°$ in θ_{HG} & ϕ_{HG} determinations and $\pm10\%$ in obtaining κ. Using θ_{HG}, ϕ_{HG}, and η_{cme} we formulate the FR axis and considering the Earth's location as $(\theta_{HG}, \phi_{HG}) = (0,0)$ we define p as

$$p = \frac{|\theta_{HG} - \phi_{HG}tan(\eta)|}{\sqrt{1 + tan^2(\eta)}}. \tag{7}$$

Using κ that constrains the FR expansion, $R_{MC}(0)$ can be determined by

$$R_{MC}(0) = \frac{height_{MC}}{1 + 1/\kappa}, \tag{8}$$

where $height_{MC}$ is the leading-edge height of MCs reaching at the Earth. Thus, it is equivalent to the Sun-Earth distance. The length (L_{MC}) of the FR axis at any heliocentric distance (r) is obtained using AW by the formula $L_{MC} = (AW \times r)$, where AW is in radian. In Figure 3(a), we show a schematic of cylindrical FR with the Sun, Earth and spacecraft positions. The CME source location ('s'), apex ('X'), tilt, angular width (AW), heliocentric distance (r), L_{MC} and p are indicated on the Figure. The centre of the Sun and Earth are denoted by 'c' and 'E', respectively. Figure 3(b) shows a South-East directed MC FR axis 'PQ' projected on the solar disk with a positive η measured anti-clockwise from the East-West direction. The Earth's location ($(\theta_{HG}, \phi_{HG}) = (0,0)$) projected on the solar disk is noted by 'E'.

2.3. Estimation of flux-rope's near-Sun magnetic properties

The magnetic field pattern of a flux rope can be expressed in terms of a "flux rope (FR) type" (Bothmer & Schwenn 1998; Mulligan et al. 1998). The FR type can be determined using FR chirality – right-handed or left-handed twist of the FR's helical magnetic field component, FR axis tilt, and the direction of FR axial magnetic field. Based on these properties, FRs are classified into eight different types including low and high-inclination FR axes. A sketch representing eight types of FRs are shown in Figure 3(a).

2.3.1. Determination of FR chirality

To estimate the handedness of FRs we analyse the Helioseismic Magnetic Imagers (HMI) line-of-sight (LOS) magnetograms, Atmospheric Imaging Assembly (AIA) images on board Solar Dynamic Observatory (SDO) and H-α images of the FRs' solar sources. The chirality of the solar source indicates the chirality of the associated FR in the corona and further out in interplanetary space as magnetic helicity is a conserved quantity even in magnetic reconnection (Berger 2005). The chirality is inferred by examining magnetic tongues (Fuentes et al. 2000; Luoni et al. 2011), dextral and sinistral natures of filament structures (Martin & McAllister 1996; Martin 2003), EUV sigmoids, skew of coronal arcades overlying the neutral lines or filament axes (McAllister et al. 1995; Martin & McAllister 1997), structure of flare-ribbons associated with CME FRs (Démoulin et al. 1996) and hemispheric helicity rule (Bothmer & Schwenn 1998). These chirality proxies are briefly discussed in Palmerio et al. (2017). Note that, the hemispheric helicity rule (see the Introduction) can be utilised to estimate CME FRs' chirality as first order approximation if CME associated solar sources are unambiguously determined.

2.3.2. Determination of flux rope type of CMEs

The orientation of the flux-rope axis roughly follows the associated PIL (Marubashi et al. 2015) or post-eruption arcades (PEAs; Yurchyshyn 2008) orientations. The flux ropes however often undergo significant rotations in the lower corona during the early evolution due to interactions with overlying skewed coronal loops (Lynch et al. 2009). To take into account the possible rotation in the corona we determine FR's axis orientation (η) from GCS at the height greater than $10 R_\odot$ from the Sun and use that in our prediction tool. We obtain the FR foot points on solar surface using EUV images and magnetograms. The foot points are determined by coronal dimming regions formed during the flux-rope rise period (Mandrini et al. 2005). We search for EUV dimming signatures in SDO/AIA 211 Å base-difference images and overlie LOS magnetogram data on them. Thus, we obtain the magnetic polarities of FR foot points. The FR axial field is directed from positive to negative foot points. In Figure 4(a) we indicate FR foot points by yellow circles on the EUV difference image obtained using observations from SDO/AIA 211 Å. The LOS magnetogram with LOS magnetic field intensity $B_{LOS} > \pm150$ G is over-plotted on the EUV difference image using red (negative magnetic field region) and green (positive magnetic field region) contours. After obtaining chirality, FR axis tilt and axial field direction we infer the flux rope type.

2.3.3. Measuring the axial magnetic field intensity (B'_0) of FRs

To estimate the axial magnetic field strength B_{CME} of CMEs near the Sun, we apply the "flux rope from eruption data" (Gopalswamy et al. 2017, FRED) technique that requires source-region reconnection flux F_{rec}, i.e., the photospheric magnetic flux under CME associated post-eruption arcades and the length (L_{CME}) & radius (R_{CME}) of CMEs. The reconnection flux is obtained using the method discussed in Gopalswamy et al. (2017a); Gopalswamy et al. (2017b). It is equivalent to the poloidal or azimuthal flux (F_{pcme}) of CME FRs (Longcope et al. 2007; Qiu et al. 2007). The poloidal flux of CMEs is conserved during their interplanetary propagation (Qiu et al. 2007; Hu et al. 2014; Gopalswamy et al. 2017a; Pal 2021) unless CME flux is significantly eroded due to reconnection in heliosphere. Thus, B'_0 is estimated using,

$$B'_0 = B_{CME} \times \frac{R_{CME}}{R_{MC}(0)}. \tag{9}$$

In Figure 4(b) a PEA region is indicated by yellow dashed line on SDO/AIA 193 Å image where the positive and negative magnetic field regions are shown by green and red contours, respectively.

2.4. Estimation of the arrival time and transit speed of CMEs

Along with magnetic profile, we estimate the CME arrival time a 1AU and transit speed utilizing a pre-existing probabilistic drag-based ensemble model (DBEMv3; Čalogović et al. 2021; Dumbović et al. 2018) – an upgraded version of a simple kinematic drag based model (DBM; Vršnak et al. 2013) established using the concept of aerodynamic drag on interplanetary propagation of CMEs. The model DBEMv3 produces possible distributions of CME arrival information by employing ensemble modeling of CME propagation. It assumes CME to be a cone structure with semicircle leading edge spanning over its angular width where the structure flattens with the CME's interplanetary evolution (Žic et al. 2015). It considers solar wind speed (V_{sw}) and drag parameter (γ) to be constant beyond the distance of 15 $R_\odot$. This is because beyond 15 $R_\odot$ CMEs propagate through an isotropic solar wind having a constant velocity. Also, the rate of the fall-off of solar wind density is similar to the rate of the self-similar expansion of CMEs (Vršnak et al. 2013; Žic et al. 2015). The DBEMv3 is available at Hvar Observatory website as an online tool (`http://phyk039240.uni-graz.at:8080/DBEMv3/dbem.php`) which is a product of European Space Agency (ESA) space situational awareness (SSA). The input to the model are CME initial speed V_{CME} with uncertainty $\pm\Delta V_{CME}$, half angular width λ projected on the plane-of-sky with uncertainty $\pm\Delta\lambda$, propagation longitude ϕ_{HG} with uncertainty $\pm\Delta\phi_{HG}$ at a specific radial distance R_0, CME arrival time t_{launch} at R_0 with uncertainty $\pm\Delta t_{launch}$ along with the radial speed of solar wind $V_{sw} \pm \Delta V_{sw}$ and drag parameter $\gamma \pm \Delta\gamma$. We prepare an ensemble of n measurements of a single CME, and m number of V_{sw} & γ using their uncertainty ranges. Thus, a total number of $n.m^2$ input sets are prepared for analysis. After performing $n.m^2$ number of runs the DBEMv3 produces distributions of $n.m^2$ number of arrival times and speeds. Here we assume that at 1 AU, the plasma propagation speed (V_{pro}) within CMEs is almost equal to its average Sun-Earth transition speed V_{tr} (Lepping et al. 2008). To prepare the inputs to DBEMv3 we utilise CME parameters obtained from GCS fitting results where the GCS model has been fitted to CMEs at a height more than $10\,R_\odot$. We derive CME initial speed V_{CME} and its arrival time at $R_0 = 21.5R_\odot$ by least-square fitting its height-time profile. Following Čalogović et al. (2021), the uncertainties Δt_{launch}, $\Delta\lambda$, and $\Delta\phi_{HG}$ are set to ±30 min, $\pm10\%$ and $\pm5°$, respectively. For each CME, the drag parameter γ is selected based on their speed. The values of γ are empirical-based, (Vršnak et al. 2013, 2014; Žic et al. 2015). For CMEs with $V_{CME} < 600$ km/s, the γ is set to $0.5 \times 10^{-7} \pm 0.1$ km^{-1}, for $600 < V_{CME} < 1000$ km/s, the γ is set to $0.2 \times 10^{-7} \pm 0.075$ km^{-1} and for $V_{CME} > 1000$ km/s the γ is set to $0.1 \times 10^{-7} \pm 0.05$ km^{-1} (Čalogović et al. 2021). To estimate the ambient solar wind speed (V_{sw}) we follow the Empirical solar wind forecast (ESWF; Vršnak & Žic 2007; Vršnak et al. 2007; Rotter et al. 2012, 2015; Reiss et al. 2016) processes that monitor fractional areas covered by coronal holes close to the central meridian region. We follow an algorithm based on an empirical relation that links the area of coronal holes appeared close to the central meridian ($\pm10°$) and solar wind speed. The empirical relationship follows the equation $V_{sw}(t) = c_0 + c_1 A(t - \delta t)$, where A is the fractional coronal hole area. We shift coronal hole area time series with a time lag δt to determine the V_{sw} at time t. Vršnak et al. (2007) studied this empirical relationship during the period DOY 25 – 125 of the year 2005 and found $\delta t = 4$ days, $c_0 = 350$ km/s and $c_1 = 900$. They found that the average relative difference between the predicted and observed peak solar wind speed valuesis $\pm10\%$. Therefore, we consider $\Delta V_{sw} = \pm10\%$

2.5. Coordinate conversion of magnetic field vectors

At 1 AU, the inclination angle (θ_{MC}) of MCs is considered to be equivalent to the η of associated CMEs and the azimuthal angle (ϕ_{MC}) of MCs are determined using CME propagation longitudes (ϕ_{HG}) obtained at 10 $R_\odot$. In order to express B_{az}, B_{ax} and B_ρ in Geocentric Solar Ecliptic (GSE) coordinate system (a Cartesian coordinate system where $\hat{z}$ is perpendicular to the Sun-Earth plane, and $\hat{x}$ is parallel to the Sun-Earth line and positive toward the Sun) that is majorly used to represent the magnetic field vectors of ICMEs at 1 AU, we transform the field vectors from local cylindrical to Cartesian coordinate system. At first B_{az}, B_{ax}, and B_ρ are converted to $B_{x,cl}$, $B_{y,cl}$ and $B_{z,cl}$ which are in local Cartesian coordinate ($\hat{x}_{cl}, \hat{y}_{cl}, \hat{z}_{cl}$) system originating at MC axis. Finally, using θ_{MC} & ϕ_{MC}, the magnetic field vectors $B_{x,cl}$, $B_{y,cl}$ and $B_{z,cl}$ are transformed to B_x, B_y and B_z.

In Figure 1, we present our MC prediction approach using a block-diagram where yellow coloured blocks represent the models and techniques used in our approach and sky-blue coloured blocks indicate the model parameters and outputs.

3. Results: Model validation using observed MC events

As a proof of concept we validate our model by investigating ten Earth-directed MCs appearing as FRs at near-Sun and in situ regions, and having clearly identified solar sources. At the near-Earth region (L1 Lagrangian point) MCs are observed using Magnetic Field Experiment (MAG) instrument of the Advanced Composition Explorer (ACE) spacecraft. The events are selected from the Richardson & Cane ICME catalog (Richardson & Cane 2010, ; `http://www.srl.caltech.edu/ACE/ASC/DATA/level3/icmetable2.html`). The front and rear boundaries of the MCs are verified manually such that at 1 AU they maintain the MC properties suggested by Burlaga et al. (1981) throughout their interval and their associated CMEs appear as isolated magnetic structures in near-Sun observations.

3.1. Preparation of model inputs

We manually identify each of the MC associated CMEs following Zhang et al. (2007); Pal et al. (2017) and locate their solar sources utilizing their coronal signatures observed in SDO/AIA. We obtain CME's geometrical parameters θ_{HG}, ϕ_{HG}, AW, η, and κ at a height $h_l > 10R_\odot$ and tabulate them in Column 5-10 of Table 1, respectively. The GCS fitting to FRs associated with Event 4 and 7 CMEs can be found in Figure 5 and 1 of Pal et al. (2017) and Pal et al. (2018), respectively. We define CME initiation time (CME_{start}) as the moment when the CMEs are first identified at SOHO/LASCO C2 field of view. In Column 1 and 2 the event numbers (Ev no.) and CME_{start} are mentioned, respectively. Column 3 and 4 contain the start (MC_{start}) and end time (MC_{end}) of MCs adapted from the Richardson & Cane ICME catalog.

Table 1. Near-Sun observations of CME latitude (θ_{HG}), longitude (ϕ_{HG}), tilt (η), aspect ratio (κ), height (h_l) of the CME leading edges and the angular width (AW), their initiation time (CME_{start}), and associated MCs' start (MC_{start}) and end times (MC_{end}).

Ev no. (1)	CME_{start} (UT) (2)	MC_{start} (UT) (3)	MC_{end} (UT) (4)	Dur_{obs} (hr) (5)	θ_{HG} (°) (6)	ϕ_{HG} (°) (7)	η (°) (8)	AW (°) (9)	κ (10)	h_l ($R_\odot$) (11)
1	2010/05/24 14:06:00	2010/05/28 20:46:00	2010/05/29 16:27:00	20	0	5.3	−53.3	36	0.22	11.4
2	2011/06/02 08:12:00	2011/06/05 01:50:00	2011/06/05 19:00:00	17	−7.8	−11.8	55.3	34	0.15	14.7
3	2012/02/10 20:00:00	2012/02/14 20:24:00	2012/02/16 05:34:00	33	28	−23	−72	50	0.23	13.5
4	2012/06/14 14:12:00	2012/06/16 22:00:00	2012/06/17 14:00:00	16	0	−5	30.7	76	0.30	15
5	2012/07/12 16:48:00	2012/07/15 06:00:00	2012/07/17 05:00:00	47	−8	14	53.1	60	0.66	14.1
6	2012/11/09 15:12:00	2012/11/13 09:44:00	2012/11/14 02:49:00	24	2.8	−4	−2	36	0.20	12.4
7	2013/03/15 07:12:00	2013/03/17 14:00:00	2013/03/18 00:45:00	11	−6.5	−10	−74.4	51	0.27	18
8	2013/04/11 07:24:00	2013/04/14 16:41:00	2013/04/15 20:49:00	28	−5.5	−15	68.2	74	0.24	20.5
9	2013/06/02 20:00:00	2013/06/06 14:23:00	2013/06/08 00:00:00	33	−1.7	7	75.5	36	0.21	12.14
10	2013/07/09 15:12:00	2013/07/13 04:39:00	2013/07/15 00:00:00	43	2	3	−37.5	36	0.36	13.4

Utilizing V_{sw} (derived using empirical relationship between coronal hole area and solar wind speed), drag parameter, CME's deprojected velocity, longitude and projected angular width and their uncertainties as input, DBEMv3 estimates the probability (p_{tar}) of CME arrival at Earth, arrival time and arrival speed distributions. The median t_{ar} of arrival time distribution with 95% confidence intervals ($t_{ar,LCI} < t_{ar} < t_{ar,HCI}$) are mentioned in Column 5 of Table 2. We compute CME transit speed V_{tr} using Sun-Earth distance and t_{ar}. The error in arrival time prediction is obtained from $t_{err} = t_{ar} - MC_{start}$. We present V_{tr} and t_{err} in Column 6 and 7. In Column 2, 3, and 4 of Table 2, we provide extrapolated deprojected speed of CMEs at 21.5 $R_\odot$, V_{sw} during CME propagation, and p_{tar}, respectively. We obtain the mean absolute error (MAE) in prediction of CME arrival time as ∼6.3 hours.

To determine FR types, we obtain their chirality, axis orientations, and axial magnetic field directions using remote observations as described before. The multi-wavelength proxies mentioned in Section 2.3.1 are examined for all MCs to infer their chirality. We convert PEA tilt and FR axis tilt η into the orientation angles η_{arcade} and η_{cme} respectively, which lie within the range $[-180°, 180°]$. The angles are measured from the solar west direction, counterclockwise for positive and clockwise for negative values. They are derived by taking into account the axial field direction that is estimated using coronal dimming information. Yurchyshyn (2008) studied the relation between PEA angles and CME directions of 25 FR events and found that for majority of events the difference between the angles remains less than 45°. In Table 3, we summarise the near-Sun FR magnetic properties of ten events. Column 1 shows the Event numbers, Column 2 shows flux-rope chirality, where '+1' stands for right-handedness and '−1' represents left-handedness. In Column 3, 4 and 5 we present η_{arcade}, η_{cme} and their difference η_{diff}, where positive value of η_{diff} represents rotation of CME axis in counterclockwise with respect to PEA tilt.

Table 2. A table containing CME speed (V_{CME}), solar wind speed (V_{SW}), probability of CME arrival at Earth (p_{tar}), predicted arrival time range ($t_{ar,LCI} < t_{ar} < t_{ar,HCI}$), predicted Sun-Earth transition speed (V_{tr}) and the difference t_{err} between the observed and predicted arrival time median values.

Ev no.	V_{CME}	V_{SW}	p_{tar}	$t_{ar,LCI} < t_{ar} < t_{ar,HCI}$	V_{tr}	t_{err}
	km/s	km/s	%	UT	km/s	Hr
(1)	(2)	(3)	(4)	(5)	(6)	(7)
1	562±60	350±35	100	228-05-2010 05:57 < 28-05-2010 10:05 < 28-05-2010 14:42	450	−10.7
2	937±20	356±36	100	04-06-2011 20:09 < 05-06-2011 00:11 < 05-06-2011 04:17	646	−1.7
3	658±13	352±35	51	14-02-2012 05:05 < 14-02-2012 09:41 < 14-02-2012 13:35	482	−10.7
4	1020±60	350±35	100	16-06-2012 13:57 < 16-06-2012 17:31 < 16-06-2012 21:00	806	−4.5
5	1000±200	363±36	100	15-07-2012 00:20 < 15-07-2012 05:42 < 15-07-2012 11:15	679	−0.3
6	611±24	350±35	100	12-11-2012 18:22 < 12-11-2012 21:22 < 13-11-2012 00:38	529	−11
7	1160±28	355±35	100	17-03-2013 02:47 < 17-03-2013 06:20 < 17-03-2013 09:59	877	−7.7
8	700±24	371±37	99.8	14-04-2013 07:55 < 14-04-2013 11:53 < 14-04-2013 16:40	599	−4.8
9	500±70	350±35	100	06-06-2013 16:42 < 06-06-2013 22:17 < 07-06-2013 04:47	383	7.9
10	610±30	350±35	100	12-07-2013 21:28 < 13-07-2013 00:37 < 13-07-2013 04:04	508	−4

Table 3. CME's near-Sun magnetic properties – PEA tilt (η_{arcade}), CME axis orientation (η_{cme}), their differences (η_{diff}), near-Sun FR type ($type_{ns}$) and axial magnetic field intensity (F_{pcme}).

Ev no.	Chirality	η_{arcade} (°)	η_{cme} (°)	η_{diff} (°)	$type_{ns}$	F_{pcme} (10^{21} Mx)
(1)	(2)	(3)	(4)	(5)	(6)	(7)
1	LH	−19.3	−53.3	−34	WSE	2.15
2	RH	46.2	55.3	9	WNE	1.81
3	RH	110.2	72	−38.2	ESW	2
4	RH	−127.4	−149.3	−22	NES	8.45
5	RH	−151	−127	24	ESW	14.10
6	RH	−172	178	−6	NES	2.47
7	RH	123	105.6	−17.4	ESW	4.10
8	LH	−61.5	−111.8	−50.3	ENW	3.72
9	LH	137.7	75.5	−62.2	WSE	1.75
10	LH	−39.2	−37.5	1.7	NWS	3.50

As η_{cme} is measured at a coronal height (≥ 10 R$_{\odot}$) greater than that where the η_{arcade} is measured, we utilise η_{cme} as the final value of FR axial orientation. Combining η_{cme}, chirality, and FR axis direction, we estimate the type of CME FRs, $type_{ns}$ and mention it in Column 6 of Table 3. Finally, the axial magnetic field intensity of the associated CMEs are derived using F_{pcme} and FR geometrical parameters. Column 7 of Table 3 shows the F_{pcme} of near-Sun FRs.

3.2. Model outputs

Using the near-Sun CME observations as input to the constant-α force-free cylindrical FR model that expands self-similarly in radial directions we estimate the magnetic field vectors of the associated MCs intersecting the spacecraft at 1 AU. To incorporate the ambiguities involved in measurements of propagation direction, inclination, and size of CMEs we utilize the uncertainty range of those parameters as input to our model. We prepare ten different random input sets of each MC where the input parameter values are within ±10° of measured propagation direction and η_{cme}, and ±10% of estimated κ value. The magnetic field vectors are derived using each of the input sets. Thus, we obtain ten different magnetic profiles for every event and measure the root-mean-square (rms) differences between observed and predicted magnetic vectors. The normalised rms difference (Δ_{rms}) is calculated using the ratio of δB and B^o_{max}, where B^o_{max} is the maximum observed magnetic field intensity and δB is defined by,

$$\delta B = \sqrt{\frac{\sum_i (\mathbf{B^o(t_i)} - \mathbf{B^p(t_i)})^2}{N}}. \tag{10}$$

Here $\mathbf{B^o(t_i)}$ and $\mathbf{B^p(t_i)}$ are the observed and predicted magnetic field vectors, respectively, and $i = 1, 2, 3...N$ with N being the total number of data points in predicted magnetic vectors. The observed magnetic field vector is binned with a bin size=($\frac{MC_{end}-MC_{start}}{N}$). We obtain MC axis orientations (θ^m_{MC}, ϕ^m_{MC}) and impact parameters corresponding to those predicted MC magnetic profiles having minimum value of Δ_{rms}. The Δ_{rms} is estimated for B_x, B_y and B_z, separately and represented by Δ^x_{rms}, Δ^y_{rms} and Δ^z_{rms}, respectively. In Figure 5 we display the predicted magnetic vectors obtained from the model along with the in situ data measured at L1 by ACE/MAG instrument for ten MCs. The observed solar wind magnetic field vectors are shown in black whereas the red curves over plotted on them during MC intervals (indicated by dashed blue vertical lines) represent the predicted fields having minimum value of Δ_{rms}. The uncertainties in predictions resulted from errors in input estimations are shown using cyan dotted curves. The latitude, longitude, normalised impact parameter $Y^m_0 = \frac{p}{R_{MC(0)}}$ corresponding to the minimum value of Δ_{rms}, i.e., Δ^m_{rms} of individual

Table 4. Latitude (θ_{MC}^{mva}, θ_{MC}^{m}) and longitude (ϕ_{MC}^{mva}, ϕ_{MC}^{m}) of MC axes derived from observed and predicted magnetic field vectors, predicted normalised impact parameters (Y_0^m), differences in observed and predicted magnetic field vectors (Δ_{rms}), near-Earth observed FR types ($type_{ne}$), comparison of near-Sun and near-Earth FR types C_{or} and minimum and maximum values of predicted duration ranges ($Dur_{pred,min} - Dur_{pred,max}$).

Ev no.	θ_{MC}^{mva} (°)	ϕ_{MC}^{mva}(°)	θ_{MC}^{m}(°)	ϕ_{MC}^{m}(°)	Y_0^m	Δ_{rms}^m	$type_{ne}$	C_{or}	$Dur_{pred,min}$-$Dur_{pred,max}$ (Hr)
(1)	(2)	(3)	(4)	(5)	(6)	(7)	(9)	(10)	(11)
1	−69	244.5	−60	273	0.5	0.07	WSE (LH)	y	27 - 41
2	45.8	193	59	281	−0.62	0.22	WNE (RH)	y	14 - 20
3	−10.5	271	-64	307	-0.2	0.1	ESW (RH)	y	33 - 43
4	−7.5	102.4	−30.6	84.1	−0.15	0.08	NES (RH)	y	19 - 22
5	−76.3	183.9	−62.7	151	0.73	0.07	ESW (RH)	y	38 - 50
6	8	83.4	3.3	84.7	−0.1	0.07	NES (RH)	y	16 - 33
7	−15.9	16	−72	297.5	0.72	0.2	SWN (RH)	n	20 - 25
8	59.8	337	74.7	304	−0.54	0.1	ENW (LH)	y	10 - 24
9	−81.7	193.2	−70.9	97.24	0.28	0.06	WSE (LH)	y	28 - 57
10	−9	284	−36	263.7	−0.53	0.05	NWS (LH)	y	35 - 57

cases are denoted by θ_{MC}^m, ϕ_{MC}^m and Y_0^m, respectively. We apply minimum variance analysis (Sonnerup & Cahill 1967) to the in situ measurements and estimate the orientation (latitude θ_{MC}^{mva}, and longitude ϕ_{MC}^{mva}) of MCs at 1 AU, in order to compare the predicted and observed orientations. In Column 2 and 3 of Table 4, we present θ_{MC}^{mva} and ϕ_{MC}^{mva} values. We mention the values of θ_{MC}^m, ϕ_{MC}^m, Y_0^m, and Δ_{rms}^m of ten MCs in Column 4, 5, 6, and 7 of Table 4, respectively. The magnetic type of the MCs ($type_{ne}$) as observed by ACE are noted in Column 9. To compare the magnetic field orientation in predicted and observed FRs at 1 AU, we utilise the parameter C_{or} in Column 8. Here 'y' and 'n' indicate a match and mismatch in field line orientation of near-Sun and near-Earth FRs, respectively. The event numbers (Ev no.) are mentioned in Column 1. Using R_{MC} and plasma propagation speed inside FRs, we estimate a range of predicted duration values (Dur_{pred}) for each FR at 1 AU. We mention the minimum ($Dur_{pred,min}$) and maximum ($Dur_{pred,max}$) values of Dur_{pred} range in Column 11 of Table 4. The observed MC duration Dur_{obs} values are mentioned in Column 5 of Table 1. By comparing the minimum and maximum values of Dur_{pred} and Dur_{obs}, it can be noticed that the Dur_{obs} of Event 1, 4 and 7 does not fall in Dur_{pred} range and is less than $Dur_{pred,min}$ by 8, 3 and 10 hours, respectively. We notice that the over-estimation in Dur_{pred} is mostly caused due to error in V_{tr} and FR radius estimations.

4. Discussion

The modelling framework presented here allows prior estimates of the magnetic field profile of MCs at 1 AU, their arrival time, average speed while crossing the Earth and duration of passage thus providing comprehensive intelligence on impending space weather events.

The approach constrains CME FRs using remote solar observations and takes into account the radial expansion of MCs. It assumes MCs to expand self-similarly during their Sun-Earth propagation. The geometric and kinematic parameters of MCs are constrained using GCS fitting to the white-light coronagraph images of associated CMEs at a height greater than 10 $R_\odot$, while their magnetic parameters are constrained using remote observations of their solar sources. Once the near-Sun CME parametrization is performed, our analytical model takes only a few seconds to predict the profiles and estimates the approximate duration of Earth-directed CMEs. The near-real time data ($\approx$ 6 hour before the current time) from LASCO and SECCHI coronagraphs are available in `https://sohoftp.nascom.nasa.gov/qkl/lasco/quicklook/level_05` and `https://stereo-ssc.nascom.nasa.gov/data/beacon/`, respectively. Also, the near-real time observations ($\approx$ 1 hour before the current time) of solar atmosphere and photospheric magnetic field from AIA and HMI on board SDO spacecraft are available in `https://sdowww.lmsal.com/suntoday_v2/` and `https://jsoc.stanford.edu/data/hmi/fits/`, respectively. Using these resources, the model is able to predict the properties of CMEs reaching the Earth within 6 hours of their initiation from the Sun. Typically, CMEs may take 15 hours to several days to reach Earth after leaving the Sun. To predict the arrival of FRs at Earth the drag-based ensemble model is applied.

We apply the CESSI-MCP modelling framework to predict the magnetic profile of ten Earth-directed CMEs having clear in situ signatures at 1 AU and remote observations of solar sources. We derive the r.m.s error between observed and predicted profiles to estimate the quality of prediction. The values of r.m.s error (see Column 7 of Table 4) suggest that for most of the cases, the predicted magnetic field magnitude and vector time series show a good agreement with in situ observations. We notice that Δ_{rms}^m for

Event 2 and 7 is greater than 2× (average ($\bar{\Delta}_{rms}^m$) ± standard deviation ($\sigma_{\Delta_{rms}^m}$)) of Δ_{rms}^m values associated with other events. Although Event 2 has similar FR type at near-Sun and near-Earth region ($type_{ns} = type_{ne} =$ WNE), there exists a significant asymmetry in its magnetic field strength between inbound (while spacecraft propagates towards MC centre) and outbound (while spacecraft propagates away from MC centre) paths which might enhance the value of Δ_{rms}^m. The asymmetry does not occur only because of FR expansion or ageing effect (Démoulin et al. 2008, 2018). Rather, most of the MC field strength asymmetry is due to non-circular cross section of FRs (Démoulin & Dasso 2009). Janvier et al. (2019); Lanabere et al. (2020) quantified the FR asymmetry C_B as

$$C_B = \frac{\int_{MC_{end}}^{MC_{start}} \frac{t - t_c}{MC_{end} - MC_{start}} B(t) dt}{\int_{MC_{end}}^{MC_{start}} B(t) dt},$$ where $B(t)$ is the magnetic field strength and $t_c = (MC_{start} + MC_{end})/2$ represents the central time.

Therefore, $|C_B|$ increases with magnetic field asymmetry and a large asymmetry is marked with $|C_B| > 0.1$ (Lanabere et al. 2020). We obtain $C_B = -0.12$ in case of Event 2, which is greater than $|\bar{C}_B| \pm \delta|C_B| = 0.04 \pm 0.04$ derived for other events. Here $|\bar{C}_B|$ and $\delta|C_B|$ indicate the mean and standard deviation of C_B values, respectively. It implies that a circular-cross section model is inappropriate to estimate its magnetic profile. In Figure 6(a) we show the in situ asymmetric magnetic field intensity B of Event 2 MC. The interval within the vertical lines represents MC interval. The FR associated with Event 7 rotates significantly while propagating from the Sun to Earth and results in a comparatively high value of Δ_{rms}^m. Due to rotation, the FR type changes from the near-Sun to near-Earth regions for this event. By comparing the θ_{MC}^{mva} and θ_{MC}^m of this event, we find that the FR changes its type from high-inclination (the central axis is more or less perpendicular to the ecliptic plane) to low-inclination (the central axis is more or less parallel to the ecliptic plane) while propagating in the interplanetary medium. Based on statistical evidence, Yurchyshyn (2008); Yurchyshyn et al. (2009) and Isavnin et al. (2013) suggested that MCs rotate towards the heliospheric current sheet (HCS; Smith 2001) so that they stay aligned with the local HCS. We consider the Wilcox solar observatory coronal field map calculated from synoptic photospheric magnetogram with a potential field model (Hoeksema et al. 1983; Hoeksema 1984) during Carrington rotation (CR) 2134 when the eruption associated with Event 7 occurred. Utilising θ_{HG} and ϕ_{HG} we infer the CME locations on the coronal field map. We observe that in order to stay aligned with the HCS the associated CME axis underwent significant rotation ($\approx 56°$) and became more or less parallel to the ecliptic plane by the time it reached at 2.5 $R_\odot$. For context, in Figure 6(b) we show a coronal map during CR 2134 obtained from `http://wso.stanford.edu/synsource1.html`. The grey solid contours represent the positive field region, whereas the dotted contours indicate the negative field region. The black thick solid line represents the location of HCS. The pink circle indicates the CME location and dotted and solid pink lines show the before and after-rotation CME axis orientation, respectively.

Sarkar et al. (2020) noted that the B_x component is more sensitive to small variations ($\pm 10°$) in the CME's propagation direction and tilt than the B_y and B_z components. They found that within the propagation direction uncertainties, the B_x component of MCs may have both positive and negative components. In our study we observe that the uncertainty in CME's direction of propagation and tilt leads to a significant variation in predicted B_x profiles of MCs associated with Event 1, 3, 4, 6 and 10 (see the blue dotted lines in the third panel of Figure 5(a), (c), (d), (f) and (j) have both positive and negative values).

For obtaining deprojected geometrical parameters and kinematics of CMEs, simultaneous observations from different vantage points in space are necessary (Bosman et al. 2012). Bosman (2016) demonstrated that to resolve a CME well globally (3-D) from 2-D plane-of-sky images obtained using coronagraphs on board spacecrafts, the angular separation ζ between the spacecrafts need to be large, i.e., $10° < \zeta \leq 90°$. If ζ is in between $0° - 10°$, the 2-D plane-of-sky images obtained from two coronagraphs on board two separate spacecrafts become nearly congruent, whereas a value of $\zeta = 90°$, provides the best condition to resolve a CME in 3-D. (Thernisien et al. 2009). The out-of-ecliptic observations of Metis: multi-wavelength coronagraph for the Solar Orbiter mission and potential L5 and L4 solar missions are expected to have significant contributions in enhancing the precision of CME parameterisation.

The presented framework to estimate the magnetic field time evolution of the near-Earth crossing of MCs, their arrival time and passage duration appears very promising. As discussed in the Introduction the capability to estimate reliably the time series of B_z is crucial for space weather forecasting.

However, this approach is not expected to perform well in some cases, e.g., the case of strongly interacting CMEs, e.g., where CMEs interact significantly with other CMEs and extraneous magnetic transients, when their propagation is influenced by fast stream originating from nearby coronal holes, when their configuration is influenced by the heliospheric current sheet and fast solar wind stream, or when their cross-sections differ strongly from a circular shape.

5. Conclusions

In this paper, we develop a scheme to predict the time series of magnetic field vectors of CME associated magnetic clouds during their near-Earth passage, estimate their arrival time, speed and duration of passage. The CESSI-MCP model is completely constrained by solar disk/near-Sun observations, is fast, has a large time window for predictions and can be easily transitioned in to operational forecasting. The ability to perform all these tasks at high fidelity, including predicting the passage duration of MCs are significant from the space weather perspective.

We believe the enhanced functional utility of our methodology is due to a combination of factors, including, constraining the CME flux rope realistically using solar observations and allowing the expansion of its cross-section. Our work emphasizes the importance of near-Sun observations, multi-vantage points observations, and in situ observations in deriving realistic intrinsic parameters of CMEs from the Sun to near-Earth.

References

Berger, M. A. 2005, Highlights of Astronomy, 13, 85
Bosman, E. 2016, PhD thesis, Georg-August-Universität Göttingen
Bosman, E., Bothmer, V., Nisticò, G., et al. 2012, Solar Physics, 281, 167
Bosman, E., Bothmer, V., Nisticò, G., et al. 2012, Solar Physics, 281, 167
Bothmer, V. & Schwenn, R. 1998, Annales Geophysicae, 16, 1
Burkepile, J. T., Hundhausen, A. J., Stanger, A. L., St.Cyr, O. C., & Seiden, J. A. 2004, Journal of Geophysical Research (Space Physics), 109
Burlaga, L. 1988, Journal of Geophysical Research (Space Physics), 93, 7217
Burlaga, L. 1991, Journal of Geophysical Research (Space Physics), 96, 5847
Burlaga, L., Sittler, E., Mariani, F., & Schwenn, R. 1981, Journal of Geophysical Research (Space Physics), 86, 6673
Burlaga, L., Sittler, E., Mariani, F., & Schwenn, R. 1981, Journal of Geophysical Research (Space Physics), 86, 6673
Čalogović, J., Dumbović, M., Sudar, D., et al. 2021, Solar Physics, 296, 1
Cook, G., Mackay, D., & Nandy, D. 2009, Astrophys. J., 704, 1021
Dal Lago, A., Schwenn, R., & Gonzalez, W. D. 2003, Advances in Space Research, 32, 2637
Démoulin, P. & Dasso, S. 2009, Astronomy & Astrophysics, 498, 551
Démoulin, P. & Dasso, S. 2009, A&A, 507, 969
Démoulin, P., Dasso, S., & Janvier, M. 2018, A&A, 619, A139
Démoulin, P., Nakwacki, M. S., Dasso, S., & Mandrini, C. H. 2008, Solar Physics, 250, 347
Démoulin, P., Nakwacki, M. S., Dasso, S., & Mandrini, C. H. 2008, Sol. Phys., 250, 347
Démoulin, P., Priest, E., & Lonie, D. 1996, Journal of Geophysical Research (Space Physics), 101, 7631
Dumbović, M., Čalogović, J., Vršnak, B., et al. 2018, The Astrophysical Journal, 854, 180
Fuentes, M. L., Démoulin, P., Mandrini, C. H., & van Driel-Gesztelyi, L. 2000, The Astrophysical Journal, 544, 540
Goldstein, H. 1983, in NASA Conference Publication, Vol. 228, NASA Conference Publication
Gonzalez, W. D., Tsurutani, B. T., & De Gonzalez, A. L. C. 1999, Space Science Reviews, 88, 529
Gopalswamy, N., Akiyama, S., Yashiro, S., & Xie, H. 2017, Proceedings of the International Astronomical Union, 13, 258
Gopalswamy, N., Akiyama, S., Yashiro, S., & Xie, H. 2017b, Journal of Atmospheric and Solar-Terrestrial Physics
Gopalswamy, N., Makela, P., Yashiro, S., & Davila, J. M. 2012, Sun and Geosphere, 7, 7
Gopalswamy, N., Yashiro, S., Akiyama, S., & Xie, H. 2017a, Solar Physics, 292, 65
Hidalgo, M. 2003, Journal of Geophysical Research (Space Physics), 108
Hoeksema, J. T. 1984, Structure and Evoluton of the Large Scale Solar and Heliospheric Magnetic Fields., Tech. rep., STANFORD UNIV CA CENTER FOR SPACE SCIENCE AND ASTROPHYSICS
Hoeksema, J. T., Wilcox, J. M., & Scherrer, P. H. 1983, Journal of Geophysical Research: Space Physics, 88, 9910
Howard, T., Nandy, D., & Koepke, A. 2008, Journal of Geophysical Research (Space Physics), 113
Hu, Q., Qiu, J., Dasgupta, B., Khare, A., & Webb, G. M. 2014, The Astrophysical Journal, 793, 53
Isavnin, A., Vourlidas, A., & Kilpua, E. K. J. 2013, Sol. Phys., 284, 203
Isavnin, A., Vourlidas, A., & Kilpua, E. K. J. 2014, Sol. Phys., 289, 2141
Janvier, M., Winslow, R. M., Good, S., et al. 2019, Journal of Geophysical Research: Space Physics, 124, 812
Kay, C. & Gopalswamy, N. 2017, Journal of Geophysical Research (Space Physics), 122, 11
Kay, C. & Opher, M. 2015, The Astrophysical Journal Letters, 811, L36
Kay, C., Opher, M., & Evans, R. M. 2015, ApJ, 805, 168
Kilpua, E., Koskinen, H. E. J., & Pulkkinen, T. I. 2017, Living Reviews in Solar Physics, 14, 5
Kilpua, E. K. J., Lugaz, N., Mays, M. L., & Temmer, M. 2019, Space Weather, 17, 498
Lanabere, V., Dasso, S., Démoulin, P., et al. 2020, Astronomy & Astrophysics, 635, A85
Lepping, R. P., Wu, C. C., Berdichevsky, D. B., & Ferguson, T. 2008, Annales Geophysicae, 26, 1919
Liu, Y., Hoeksema, J., Bobra, M., et al. 2014, The Astrophysical Journal, 785, 13
Longcope, D., Beveridge, C., Qiu, J., et al. 2007, Solar Physics, 244, 45
Lundquist, S. 1951, Phys. Rev., 83, 307
Luoni, M. L., Démoulin, P., Mandrini, C. H., & van Driel-Gesztelyi, L. 2011, Solar Physics, 270, 45
Lynch, B., Antiochos, S., Li, Y., Luhmann, J., & DeVore, C. 2009, The Astrophysical Journal, 697, 1918
Manchester, W., Kilpua, E. K. J., Liu, Y. D., et al. 2017, Space Science Reviews, 212, 1159
Manchester, W. B., Gombosi, T. I., Roussev, I., et al. 2004, Journal of Geophysical Research (Space Physics), 109, A02107
Manchester, W. B., van der Holst, B., & Lavraud, B. 2014, Plasma Physics and Controlled Fusion, 56, 064006
Mandrini, C. H., Pohjolainen, S., Dasso, S., et al. 2005, Astronomy & Astrophysics, 434, 725
Martin, S. & McAllister, A. 1996, in Magnetodynamic phenomena in the solar atmosphere (Springer), 497–498
Martin, S. & McAllister, A. 1997, Washington DC American Geophysical Union Geophysical Monograph Series, 99, 127
Martin, S. F. 2003, Advances in Space Research, 32, 1883
Marubashi, K. 1986, Advances in Space Research, 6, 335
Marubashi, K. 1997, Coronal mass ejections, 99, 147
Marubashi, K., Akiyama, S., Yashiro, S., et al. 2015, Solar Physics, 290, 1371
Marubashi, K. & Lepping, R. P. 2007, Annales Geophysicae, 25, 2453
McAllister, A., Hundhausen, A., Burkpile, J., McIntosh, P., & Hiei, E. 1995, in Bulletin of the American Astronomical Society, Vol. 27, 961
Möstl, C., Amerstorfer, T., Palmerio, E., et al. 2018, Space Weather, 16, 216
Möstl, C., Rollett, T., Frahm, R. A., et al. 2015, Nature Communications, 6, 7135
Mulligan, T., Russell, C., & Luhmann, J. 1998, Geophysical Research Letters, 25, 2959
Nandy, D. 2006, Journal of Geophysical Research: Space Physics, 111
Nieves-Chinchilla, T., Vourlidas, A., Raymond, J., et al. 2018, Solar Physics, 293, 1
Osherovich, V., Farrugia, C., & Burlaga, L. 1993, Journal of Geophysical Research (Space Physics), 98, 13225
Pal, S. 2021, Advances in Space Research
Pal, S., Dash, S., & Nandy, D. 2020, Geophysical Research Letters, 47, e2019GL086372
Pal, S., Gopalswamy, N., Nandy, D., et al. 2017, Astrophys. J., 851, 123
Pal, S., Nandy, D., Srivastava, N., Gopalswamy, N., & Panda, S. 2018, The Astrophysical Journal, 865, 4
Palmerio, E., Kilpua, E. K., James, A. W., et al. 2017, Solar Physics, 292, 39
Palmerio, E., Kilpua, E. K., Möstl, C., et al. 2018, Space Weather, 16, 442
Pevtsov, A. & Balasubramaniam, K. 2003, Advances in Space Research, 32, 1867
Qiu, J., Hu, Q., Howard, T. A., & Yurchyshyn, V. B. 2007, The Astrophysical Journal, 659, 758
Reiss, M. A., Temmer, M., Veronig, A. M., et al. 2016, Space Weather, 14, 495
Richardson, I. G. & Cane, H. V. 2010, Solar Physics, 264, 189
Rotter, T., Veronig, A., Temmer, M., & Vršnak, B. 2012, Solar Physics, 281, 793
Rotter, T., Veronig, A., Temmer, M., & Vršnak, B. 2015, Solar Physics, 290, 1355
Sarkar, R., Gopalswamy, N., & Srivastava, N. 2020, The Astrophysical Journal, 888, 121

Savani, N. P., Vourlidas, A., Szabo, A., et al. 2015, Space Weather, 13, 374

Schrijver, C. J., Kauristie, K., Aylward, A. D., et al. 2015, Advances in Space Research, 55, 2745

Schwenn, R., dal Lago, A., Huttunen, E., & Gonzalez, W. D. 2005, Annales Geophysicae, 23, 1033

Scolini, C., Dasso, S., Rodriguez, L., Zhukov, A. N., & Poedts, S. 2021, arXiv e-prints, arXiv:2102.07569

Shen, C., Wang, Y., Pan, Z., et al. 2013, Journal of Geophysical Research (Space Physics), 118, 6858

Shen, F., Shen, C., Zhang, J., et al. 2014, Journal of Geophysical Research: Space Physics, 119, 7128

Shimazu, H. & Vandas, M. 2002, Earth, planets and space, 54, 783

Smith, E. J. 2001, Journal of Geophysical Research: Space Physics, 106, 15819

Sonnerup, B. U. O. & Cahill, L. J., J. 1967, J. Geophys. Res., 72, 171

Subramanian, P., Arunbabu, K., Vourlidas, A., & Mauriya, A. 2014, The Astrophysical Journal, 790, 125

Thernisien, A. 2011, The Astrophysical Journals, 194, 33

Thernisien, A., Vourlidas, A., & Howard, R. A. 2009, Solar Physics, 256, 111

Thernisien, A. F. R., Howard, R. A., & Vourlidas, A. 2006, The Astrophysical Journal, 652, 763

Tsurutani, B. T., Gonzalez, W. D., Tang, F., Akasofu, S. I., & Smith, E. J. 1988, Journal of Geophysical Research (Space Physics), 93, 8519

Vandas, M., Romashets, E., & Geranios, A. 2015, Astronomy & Astrophysics, 583, A78

Vandas, M., Romashets, E., Watari, S., et al. 2006, Advances in Space Research, 38, 441

Vourlidas, A., Balmaceda, L. A., Stenborg, G., & Dal Lago, A. 2017, ApJ, 838, 141

Vourlidas, A., Colaninno, R., Nieves-Chinchilla, T., & Stenborg, G. 2011, The Astrophysical Journal Letters, 733, L23

Vršnak, B., Amerstorfer, T., Dumbović, M., et al. 2019, The Astrophysical Journal, 877, 77

Vršnak, B., Temmer, M., & Veronig, A. M. 2007, Solar Physics, 240, 315

Vršnak, B., Temmer, M., Žic, T., et al. 2014, The Astrophysical Journal Supplement Series, 213, 21

Vršnak, B. & Žic, T. 2007, Astronomy & Astrophysics, 472, 937

Vršnak, B., Žic, T., Vrbanec, D., et al. 2013, Solar physics, 285, 295

Vršnak, B., Žic, T., Vrbanec, D., et al. 2013, Solar Physics, 285, 295

Wang, Y., Shen, C., Wang, S., & Ye, P. 2004, Solar Physics, 222, 329

Wang, Y., Shen, C., Wang, S., & Ye, P. 2004, Sol. Phys., 222, 329

Wang, Y., Wang, B., Shen, C., Shen, F., & Lugaz, N. 2014, Journal of Geophysical Research (Space Physics), 119, 5117

Webb, D. F. & Howard, T. A. 2012, Living Reviews in Solar Physics, 9, 3

Yeates, A., Attrill, G., Nandy, D., et al. 2010, The Astrophysical Journal, 709, 1238

Yurchyshyn, V. 2008, The Astrophysical Journal Letters, 675, L49

Yurchyshyn, V., Abramenko, V., & Tripathi, D. 2009, The Astrophysical Journal, 705, 426

Zhang, J., Richardson, I. G., Webb, D. F., et al. 2007, Journal of Geophysical Research (Space Physics), 112, A12103

Žic, T., Vršnak, B., & Temmer, M. 2015, The Astrophysical Journal Supplement Series, 218, 32
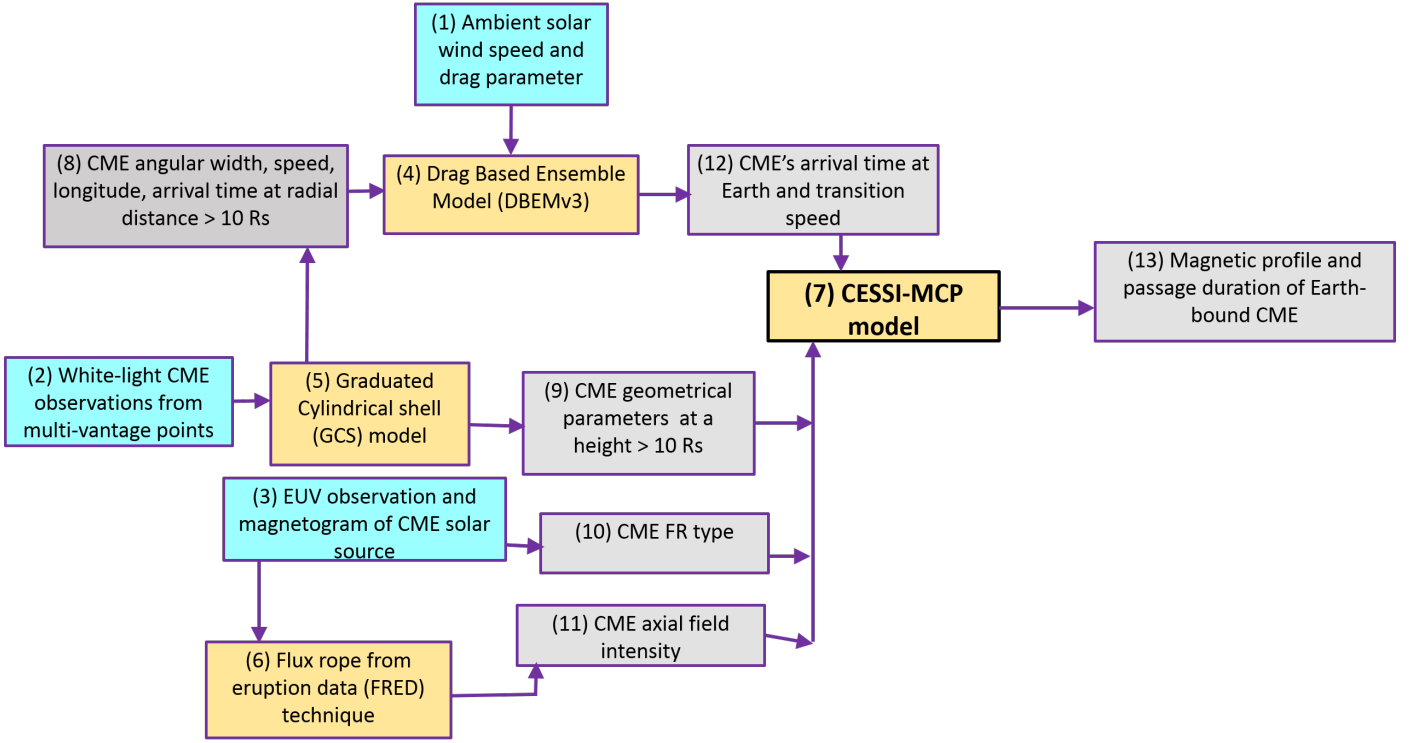
Fig. 1. A block-diagram representing the steps involved in our analytical approach to predict Earth-bound CME magnetic vectors and passage duration. The cyan blocks 1–3 contain remote near-Sun observations used as inputs, The yellow blocks 4–7 indicate the analytical, empirical models and techniques involved in our approach. The grey blocks 8–13 indicate the outputs.
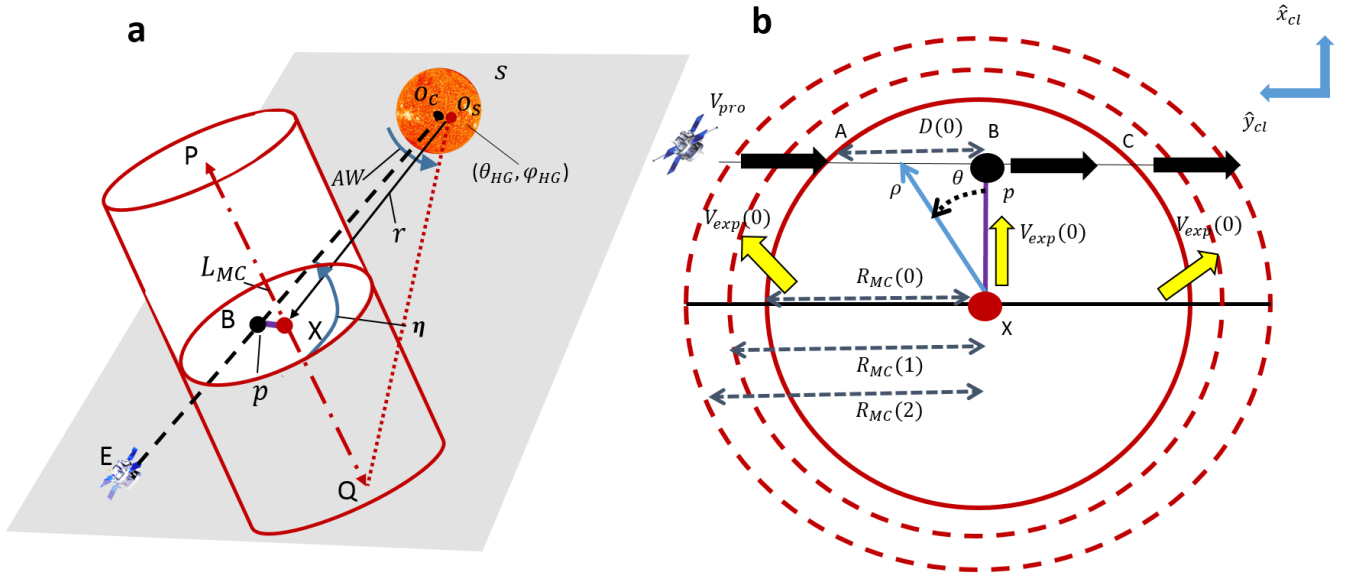

Fig. 2. (a) A schematic of cylindrical MC (firm red curve), ecliptic plane (grey), the position of the Sun 'S' and the spacecraft 'E' at L1. The AW, η_{cme}, Sun-center 'O_c' and CME source location 'O_s' on solar disk are mentioned on the figure. The FR axis is shown in red dash-dotted line. The Sun-Earth line 'O_cE' is shown by black dashed line and it is on the ecliptic plane. The lines 'O_sX' and 'PQ' indicate heliocentric distance r and L_{MC}, respectively. The perpendicular distance p is denoted by the violet line 'XB'. The line 'BX' is perpendicular to 'O_cE'. (b) The expanding circular cross section of a cylindrical MC. 'O' is the centre of the cross section. At $t = 0$ the MC's cross sectoral circumference is denoted by a red circle. The MC's radial expansion with a speed V_{exp} is in the direction of the yellow arrows and the spacecraft propagates with a speed V_{pro} towards the path indicated by black arrows.
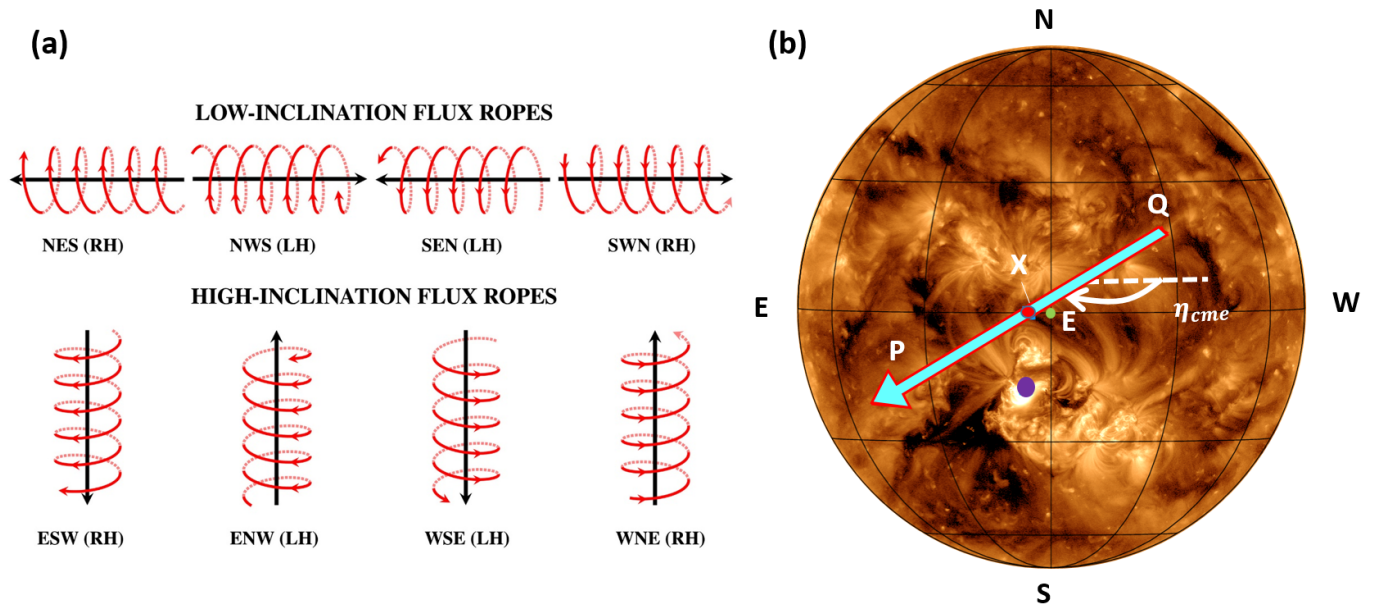
.

Fig. 3. (a) A sketch representing eight types of FRs. For each type, the heilcal and axial field lines are shown in red and black, respectively. Each letter of the name of the type of FRs corresponds to one of four directions, i.e., North, South, East, West, (ex. - NES - North-East-South) and RH and LH denote right-handed and left-handed chirality, respectively. The first and last letters indicate the helical field directions and the letter in between indicates the FR's axial field direction. The image is adapted from Palmerio et al. (2018) (b) A South-East directed axis of CME ('PQ') similar to the FR of Event 4 shown in cyan line projected on the solar disk. Its apex is denoted by a red dot 'X'. The CME's solar source ('O_s') is indicated by a violet dot and the projected location of the Earth ('E') on the solar disk is denoted by a green dot. The axis has a negative value of η_{cme} with respect to the East-West line. The η_{cme} and η_{arcade} associated with this FR is -149 and -127, respectively.
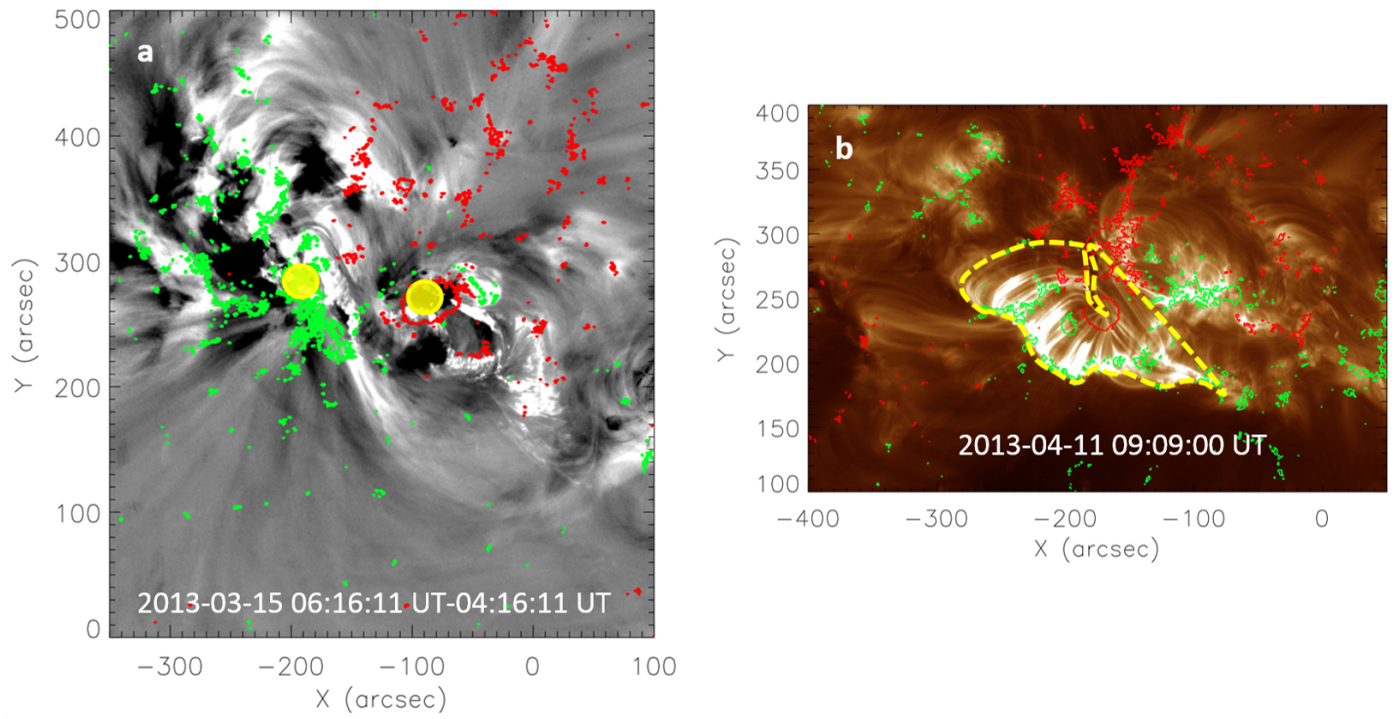
Fig. 4. Determination of CME Magnetic parameters – foot points and magnetic field intensity. (a) An EUV base difference image obtained using SDO/AIA 211 Å observations. The regions rounded by yellow circles denote FR foot points. (b) An observation of a PEA in SDO/AIA 193 Å. The PEA foot points are indicated by yellow dotted lines. In both the images, the associated LOS magnetograms with LOS magnetic field intensity $B_{LOS} > \pm 150$ G are over-plotted using green (positive magnetic field) and red (negative magnetic field) contours.
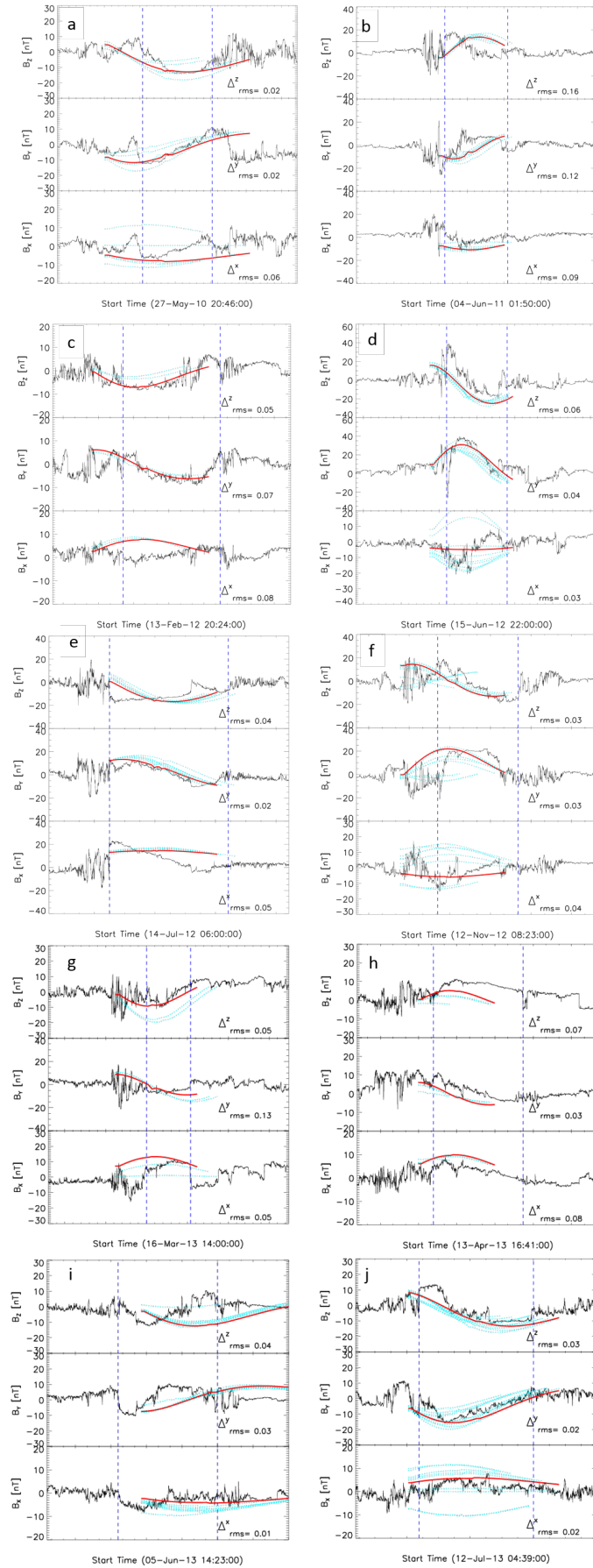.

Fig. 5. Magnetic vectors (in black) of ten MCs as observed by ACE spacecraft. The red curves represent the predicted magnetic vectors having best match with observed magnetic vectors. The cyan dotted curves show uncertainty in predictions. The blue vertical dashed lines denote the start and end time of MCs. The rms differences Δ_{rms}^x, Δ_{rms}^y, and Δ_{rms}^z between observed and predicted magnetic vectors B_x, B_y, and B_z are mentioned on the plot.
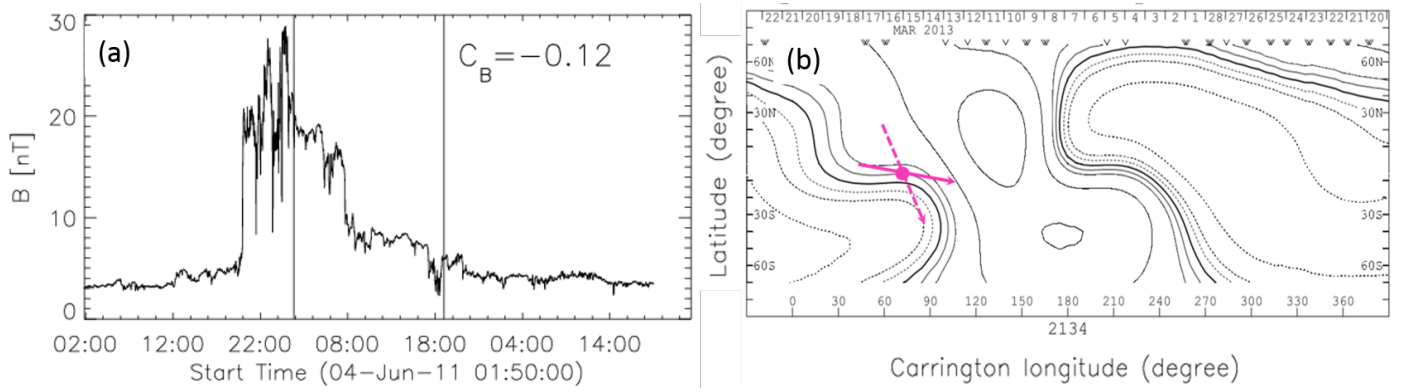
Fig. 6. (a) Asymmetry in in situ magnetic field intensity associated with Event 2 MC. The FR asymmetry parameter C_B is mentioned on the figure. The vertical lines represent the start and end times of the MC. (b) A coronal map during CR 2134 collected from Wilcox solar observatory. The grey contours represent the positive field region and the dotted contours indicate the negative field region. The HCS is represented by the black thick solid line. The pink circle indicates the location of the CME associated with Event 7. The dashed and solid pink lines show the before and after-rotation CME axis orientations, respectively.

.